arXiv:1412.0813v3 [hep-ph] 7 Apr 2015

WPCF 2014

Gyöngyös, Hungary

Excitation function of elastic pp scattering
from a unitarily extended Bialas-Bzdak model

F. Nemes[1,2]

[1] CERN, CH-1211 Geneva 23, Switzerland

T. Csörgő[2,3]

[2] Wigner Research Centre for Physics, Hungarian Academy of Sciences
H-1525 Budapest 114, P.O.Box 49, Hungary
[3]KRF, H-3200 Gyöngyös, Mátrai út 36, Hungary

M. Csanád[4]

[4] Eötvös University, Department of Atomic Physics
H-1117 Budapest, Pázmány Péter s., 1/A Hungary

August 22, 2018

Abstract

The Bialas-Bzdak model of elastic proton-proton scattering assumes a
purely imaginary forward scattering amplitude, which consequently van-
ishes at the diffractive minima. We extended the model to arbitrarily large
real parts in a way that constraints from unitarity are satisfied. The re-
sulting model is able to describe elastic pp scattering not only at the lower
ISR energies but also at $\sqrt{s} =7$ TeV in a statistically acceptable manner,
both in the diffractive cone and in the region of the first diffractive min-
imum. The total cross-section as well as the differential cross-section of

1

elastic proton-proton scattering is predicted for the future LHC energies of $\sqrt{s}$ =8, 13, 14, 15 TeV and also to 28 TeV. A non-trivial, significantly non-exponential feature of the differential cross-section of elastic proton-proton scattering is analyzed and the excitation function of the non-exponential behavior is predicted. The excitation function of the shadow profiles is discussed and related to saturation at small impact parameters.

1   Introduction

In a pair of recent papers the Bialas-Bzdak model [1] (BB) of small angle elastic proton-proton (pp) scattering at high energies was studied at 7 TeV LHC energy [2,3]. In those papers a terse overview is reported about the field of elastic scattering at high energies. Here we would like to highlight only some recent works which influenced us.

In this manuscript the BB model is extrapolated to future LHC energies. Our method to include the energy evolution of the parameters is somewhat similar to the so-called "geometric scaling" discussed in Ref. [4] and also in Ref. [5].

Using 2012 data the TOTEM experiment recently made an important experimental observation at $\sqrt{s} = 8$ TeV: the pp elastic differential cross-section shows a deviation from the most simple non-exponential behavior at low-$|t|$, [6] where t is the squared four-momentum transfer of the pp scattering process. This feature of the $\sqrt{s} = 8$ TeV (preliminary) TOTEM dataset, was related to t-channel unitarity of the forward scattering amplitude (FSA) in Ref. [7], a concept that we also focus on, using and generalizing in a unitary manner the quark-diquark model of Bialas and Bzdak for the determination of the shape of the FSA of elastic pp scattering.

In its original form, the BB model [1] assumes that the real part of the FSA is negligible, correspondingly, the FSA vanishes at the diffractive minima. At the ISR energies of $\sqrt{s}$ =23.5−62.5 GeV, that were first analyzed in the inspiring paper of Bialas and Bzdak [1], this assumption is indeed reasonable, as confirmed in Ref. [2]. At these ISR energies, only very few data points were available in the dip region around the first diffractive minimum of elastic pp scattering, which were then left out from the BB model fits of Ref. [2] to achieve a quality description of the remaining data points. However, in recent years, TOTEM data [8] explored the dip region at the LHC energy of 7 TeV in great details, at several different values of the squared four-momentum transfer t. Ref. [2] demonstrated, that the original BB model cannot describe this dip region, not without at least a small real part that has to be added to its FSA in a reasonable way.

Subsequently, the BB model has been generalized in Ref. [3] by allowing for a perturbatively small real part of the FSA, which improved the agreement of the model with TOTEM data on elastic pp scattering at the LHC energy of $\sqrt{s} = 7$ TeV. It was expected that the main reason for the appearance of this real part is that certain rare elastic scattering of the constituents of the protons

may be non-collinear thus may lead to inelastic events even if the elementary interactions are elastic. The corresponding phenomenological generalization of the Bialas-Bzdak model [3] was indeed based on the assumption that the real part of the FSA is small, and can be handled perturbatively. The resulting α-generalized Bialas-Bzdak (αBB) model was compared to ISR data in Ref. [3], and it was demonstrated that a small, of the order of 1 % real part of the FSA indeed results in excellent fit qualities and a statistically acceptable description of the data in the region of the diffractive minimum or dip. However, at the LHC energy of 7 TeV, the same αBB model does not result in a satisfactory, statistically acceptable fit quality, although the visual quality of the fitted curves improve significantly as compared to that of the original BB model [3].

These results indicate that at the LHC energies the real part of the FSA may reach significant values where unitarity constraints may already play an important role. The unitarity of the S-matrix provides also the basis for the optical theorem, which in turn provides a method to determine the total cross-section from an extrapolation of the elastic scattering measurements to the $t = 0$ point.

In the αBB model of Ref. [3], unitarity constraints were not explicitly considered: as the original BB model with zero real parts obeyed unitarity, adding a small real part may possibly resulted only in small violations of unitarity and the optical theorem. However, when the model was fitted to the 7 TeV TOTEM data in the dip region in Ref. [3], the extrapolation to the point of $t = 0$ and the related value of the total cross-section underestimated the measured total cross-section by about 40%, suggesting, that perhaps the real part of the FSA may be large, and unitarity relations should be explicitly considered.

These indications motivate the present manuscript, where the Bialas-Bzdak model is further generalized to arbitrarily large real parts of the FSA, fully taking into account unitarity constraints. The resulting model is referred to as the real extended Bialas-Bzdak (ReBB) model.

The structure of the manuscript is as follows: in Section 2, the general form of the forward scattering amplitude is re-derived for the case of a non-vanishing real part starting from S-matrix unitarity. Then this result is applied to the extension of the BB model to a non-vanishing and possibly large real part of the FSA.

In Section 3, the resulting ReBB model is fitted to TOTEM data on elastic pp scattering at $\sqrt{s} = 7$ TeV, both in the diffractive cone [9, 10] and in the dip region [8], separately.

Based on these fits and comparisons of the ReBB model to $\sqrt{s} = 7$ TeV data, in Section 4.1 the shadow profile function A(b) is evaluated. This function characterizes the probability of inelastic pp scattering at a given impact parameter b, and is compared to the shadow profile functions of elastic pp collisions at lower, ISR energies. Section 4.2 is devoted to study the structure of the differential cross-section $d\sigma/dt$ at low-$|t|$ values and also to compare it with a purely exponential behavior.

In Section 5, the excitation function of the fit parameters is investigated and their evolution with $\sqrt{s}$ is obtained based on a geometrical picture. The model

3

parameters are extrapolated to the expected future LHC energies of 8, 13, 14 and 15 TeV, as well as for 28 TeV, that is not foreseen to be available at man-made accelerators in the near future, but may be relevant for the investigation of cosmic ray events. The excitation functions of the shadow profile functions $A(b)$ are also discussed. Finally we summarize and conclude.

2   The real extended Bialas-Bzdak model

Although the original form of the Bialas-Bzdak model neglects the real part of the FSA in high energy elastic pp scattering, the model is based on Glauber scattering theory and obeys unitarity constraints.

    The phenomenological generalization of the Bialas-Bzdak model [3] is based on the assumption, that the real part of the FSA is small, and can be handled perturbatively, so unitarity constraints are not violated strongly. However, it turned out that the addition of a small real part does not lead to a statistically acceptable description of TOTEM data on elastic pp collisions at $\sqrt{s} = 7$ TeV. In this manuscript, we consider the case, when the real part of the FSA is not perturbatively small. We restart from S-matrix unitarity, and consider how the BB model can be extended to significant, real values of the FSA while satisfying the constraints of unitarity.

2.1   S-matrix unitarity in the context of elastic proton-proton scattering

In this subsection some of the basic equations of quantum scattering theory are recapitulated. The scattering or S matrix describes how a physical system changes in a scattering process. The unitarity of the S matrix ensures that the sum of the probabilities of all possible outcomes of the scattering process is one.

    The unitarity of the scattering matrix S is expressed by the equation

$$SS^{\dagger} = I \,, \tag{1}$$

where I is the identity matrix. The decomposition $S = I + iT$, where T is the transition matrix, leads the unitarity relation Eq. (1) to

$$T - T^{\dagger} = iTT^{\dagger} \,, \tag{2}$$

which can be rewritten in the impact parameter b representation as

$$2\,\mathrm{Im}\,t_{el}(s,b) = |t_{el}(s,b)|^2 + \tilde{\sigma}_{inel}(s,b) \,, \tag{3}$$

where s is the squared total center-of-mass energy.

    The functions $\tilde{\sigma}_{inel}(s,b) = d^2\sigma_{inel}/d^2b$ and $|t_{el}(s,b)|^2 = d^2\sigma_{el}/d^2b$ are the inelastic and elastic scattering probabilities per unit area, respectively. The elastic amplitude $t_{el}(s,b)$ is defined in the impact parameter space and corresponds to the ℓth partial wave amplitude $T_{\ell}(s)$ through the relation $\ell + 1/2 \leftrightarrow b\sqrt{s}/2$, which is valid in the high energy limit, $\sqrt{s} \to \infty$.

4

The unitarity relation (3) is a second order polynomial equation in terms of the (complex) elastic amplitude $t_{el}(s,b)$. If one introduces the opacity or eikonal function [11–16]

$$t_{el}(s,b) = i\left[1 - e^{-\Omega(s,b)}\right],\qquad(4)$$

$\tilde{\sigma}_{inel}$ can be expressed as

$$\tilde{\sigma}_{inel}(s,b) = 1 - e^{-2\,\mathrm{Re}\,\Omega(s,b)}.$$

The formula for t_{el} is the so called eikonal form. From Eq. (4) the real part of the opacity function $\Omega(s,b)$ can be expressed as

$$\mathrm{Re}\,\Omega(s,b) = -\frac{1}{2}\ln\left[1 - \tilde{\sigma}_{inel}(s,b)\right].\qquad(5)$$

In the original BB model it is assumed that the real part of t_{el} vanishes. In this case Eqs. (4) and (5) implies that

$$t_{el}(s,b) = i\left[1 - \sqrt{1 - \tilde{\sigma}_{inel}(s,b)}\right].\qquad(6)$$

If the imaginary part $\mathrm{Im}\,\Omega$ is taken into account in Eq. (4) the result is

$$t_{el}(s,b) = i\left[1 - e^{-i\,\mathrm{Im}\,\Omega(s,b)}\sqrt{1 - \tilde{\sigma}_{inel}(s,b)}\right],\qquad(7)$$

where the concrete parametrization of $\mathrm{Im}\,\Omega(s,b)$ is discussed later.

To compare the model with data the amplitude Eq. (7) has to be transformed into momentum space

$$T(s,\Delta) = \int\limits_{-\infty}^{+\infty}\int\limits_{-\infty}^{+\infty} e^{i\vec{\Delta}\cdot\vec{b}}t_{el}(s,b)\mathrm{d}^2b\qquad(8)$$

$$= 2\pi i\int\limits_0^{\infty} J_0\left(\Delta\cdot b\right)\left[1 - e^{-\Omega(s,b)}\right]b\,\mathrm{d}b,\qquad(9)$$

where $b = |\vec{b}|$, $\Delta = |\vec{\Delta}|$ is the transverse momentum and J_0 is the zero order Bessel-function of the first kind. In the high energy limit, $\sqrt{s} \to \infty$, $\Delta(t) \simeq \sqrt{-t}$ where t is the squared four-momentum transfer. Consequently the elastic differential cross-section can be evaluated as

$$\frac{\mathrm{d}\sigma}{\mathrm{d}t} = \frac{1}{4\pi}|T(s,\Delta)|^2.\qquad(10)$$

According to the optical theorem the total elastic cross-section is

$$\sigma_{tot} = 2\,T(s,\Delta)|_{t=0},\qquad(11)$$

while the ratio of the real to the imaginary FSA is

$$\rho = \frac{\mathrm{Re}\,T(s,0)}{\mathrm{Im}\,T(s,0)}.\qquad(12)$$

5

2.2 The Bialas-Bzdak model with a unitarily extended amplitude

The original BB model [1] describes the proton as a bound state of a quark and a diquark, where both constituents have to be understood as "dressed" objects that effectively include all possible virtual gluons and $q\bar{q}$ pairs to valence or dressed quarks. The quark and the diquark are characterized with their positions with respect to the proton's center of mass using their transverse position vectors $\vec{s}_q$ and $\vec{s}_d$ in the plane perpendicular to the proton's incident momentum. Hence, the coordinate space H of the colliding protons is spanned by the vector $h = (\vec{s}_q, \vec{s}_d, \vec{s}'_q, \vec{s}'_d)$ where the primed coordinates indicate the coordinates of the second proton.

The inelastic proton-proton scattering probability $\tilde{\sigma}_{inel}(b)$ in Eq. (6) is calculated as an average of "elementary" inelastic scattering probabilities $\sigma(h; \vec{b})$ over the coordinate space H [17]

$$\tilde{\sigma}_{inel}(b) = \left\langle \sigma(h; \vec{b}) \right\rangle_H = \int\limits_{-\infty}^{+\infty} ... \int\limits_{-\infty}^{+\infty} \mathrm{d}h \, p(h) \cdot \sigma(h; \vec{b}), \tag{13}$$

where the weight function $p(h)$ is a product of probability distributions

$$p(h) = D(\vec{s}_q, \vec{s}_d) \cdot D(\vec{s}'_q, \vec{s}'_d). \tag{14}$$

The $D(\vec{s}_q, \vec{s}_d)$ function is a two-dimensional Gaussian, which describes the center of mass distribution of the quark and diquark with respect to the center of mass of the proton

$$D(\vec{s}_q, \vec{s}_d) = \frac{1 + \lambda^2}{R_{qd}^2 \, \pi} e^{-(s_q^2 + s_d^2)/R_{qd}^2} \delta^2(\vec{s}_d + \lambda \vec{s}_q), \ \lambda = \frac{m_q}{m_d}. \tag{15}$$

The parameter R_{qd}, the standard deviation of the quark and diquark distance, is fitted to the data. Note that the two-dimensional Dirac δ function preserves the proton's center of mass and reduces the dimension of the integral in Eq. (13) from eight to four.

Note that the original BB model is realized in two different ways: in one of the cases, the diquark structure is not resolved. This is referred to as the $p = (q, d)$ BB model. A more detailed variant is when the diquark is assumed to be a composition of two quarks, referred as the $p = (q, (q, q))$. Our earlier studies using the αBB model indicated [3], that the $p = (q, d)$ case gives somewhat improved confidence levels as compared to the $p = (q, (q, q))$ case. So for the present manuscript we discuss results using the $p = (q, d)$ scenario only, however, it is trivial to extend the investigations to the $p = (q, (q, q))$ case and they result in fits which are not acceptable at $\sqrt{s} = 7$ TeV. For the case of brevity we do not present the results of the analysis with the $p = (q, (q, q))$ variant of the ReBB model, only the fit quality is reported.

It is assumed that the "elementary" inelastic scattering probability $\sigma(h;\vec{b})$ can be factorized in terms of binary collisions among the constituents with a Glauber expansion

$$\sigma(h;\vec{b}) = 1 - \prod_a \prod_b \left[1 - \sigma_{ab}(\vec{b} + \vec{s}_a' - \vec{s}_b)\right], \quad a, b \in \{q, d\}, \tag{16}$$

where the indices a and b can be either quark q or diquark d.

The $\sigma_{ab}(\vec{s})$ functions describe the probability of binary inelastic collision between quarks and diquarks and are assumed to be Gaussian

$$\sigma_{ab}(\vec{s}) = A_{ab}e^{-s^2/S_{ab}^2}, \ S_{ab}^2 = R_a^2 + R_b^2, \quad a, b \in \{q, d\}, \tag{17}$$

where the R_q, R_d and A_{ab} parameters are fitted to the data.

The inelastic cross-sections of quark, diquark scatterings can be calculated by integrating the probability distributions Eq. (17) as

$$\sigma_{ab,\text{inel}} = \int_{-\infty}^{+\infty} \int_{-\infty}^{+\infty} \sigma_{ab}(\vec{s}) \, d^2s = \pi A_{ab} S_{ab}^2. \tag{18}$$

In order to reduce the number of free parameters, it is assumed that the ratios of the inelastic cross-sections $\sigma_{ab,\text{inel}}$ satisfy

$$\sigma_{qq,\text{inel}} : \sigma_{qd,\text{inel}} : \sigma_{dd,\text{inel}} = 1 : 2 : 4, \tag{19}$$

which means that in the BB model the diquark contains twice as many partons than the quark and also that these quarks and diquarks do not "shadow" each other during the scattering process. This assumption is not trivial. The $p = (q, (q, q))$ version of the BB model allows for different $\sigma_{qq,\text{inel}} : \sigma_{qd,\text{inel}} : \sigma_{dd,\text{inel}}$ ratios. However, as it was mentioned before, the $p = (q, (q, q))$ is less favored by the data as compared to the $p = (q, d)$ case presented below.

Using the inelastic cross-sections Eq. (18) together with the assumption Eq. (19) the A_{qd} and A_{dd} parameters can be expressed with A_{qq}

$$A_{qd} = A_{qq} \frac{4R_q^2}{R_q^2 + R_d^2}, \ A_{dd} = A_{qq} \frac{4R_q^2}{R_d^2}. \tag{20}$$

In this way only five parameters have to be fitted to the data R_{qd}, R_q, R_d, λ, and A_{qq}. In practice we fix $A_{qq} = 1$ assuming that head on quark-quark (qq) collisions are completely inelastic according to Eq. (17).

The last step in the calculation is to perform the Gaussian integrals in the average Eq. (13) to obtain a formula for $\tilde{\sigma}_{inel}(b)$. The Dirac δ function in Eq. (15) expresses the protons' diquark position vectors as a function of the quarks position

$$\vec{s}_d = -\lambda \, \vec{s}_q, \ \vec{s}_d' = -\lambda \, \vec{s}_q'. \tag{21}$$

After expanding the products in the Glauber expansion Eq. (16) the following sum of contributions is obtained

$$\sigma(h;\vec{b}) = \sigma_{qq} + 2 \cdot \sigma_{qd} + \sigma_{dd} - (2\sigma_{qq}\sigma_{qd} + \sigma_{qd}^2 + \sigma_{qq}\sigma_{dd} + 2\sigma_{qd}\sigma_{dd})$$
$$+ (\sigma_{qq}\sigma_{qd}^2 + 2\sigma_{qq}\sigma_{qd}\sigma_{dd} + \sigma_{dd}\sigma_{qd}^2) - \sigma_{qq}\sigma_{qd}^2\sigma_{dd}\,, \tag{22}$$

where the arguments of the $\sigma_{ab}(\vec{s})$ functions are suppressed to abbreviate the notation.

The average over H in Eq. (13) has to be calculated for each term in the above expansion Eq. (22). Take the last, most general, term and calculate the average; the remaining terms are simple consequences of it. The result is

$$I = \left\langle -\sigma_{qq}\sigma_{qd}^2\sigma_{dd} \right\rangle_H = \int\limits_{-\infty}^{+\infty} \cdots \int\limits_{-\infty}^{+\infty} \mathrm{d}h\, p(h) \cdot (-\sigma_{qq}\sigma_{qd}^2\sigma_{dd})\,, \tag{23}$$

where the $p(h)$ weight function Eq. (14) is a product of the quark-diquark distributions, given by Eq. (15). Substitute into this result Eq. (23) the definitions of the quark-diquark distributions Eq. (15)

$$I = -\frac{4v^2}{\pi^2} \int\limits_{-\infty}^{+\infty}\int\limits_{-\infty}^{+\infty} \mathrm{d}^2 s_q \mathrm{d}^2 s'_q\, e^{-2v\left(s_q^2 + s_q'^2\right)} \prod_k\prod_l \sigma_{kl}(\vec{b} - \vec{s}_k + \vec{s}'_l), \quad k,l \in \{q,d\}\,, \tag{24}$$

where $v = (1 + \lambda^2)/(2 \cdot R_{qd}^2)$ and the integral over the coordinate space H is explicitly written out; it is only four dimensional due to the two Dirac δ functions in $p(h)$. Using the definitions of the $\sigma_{ab}(\vec{s})$ functions Eq. (17) and the expression $A = A_{qq}A_{qd}A_{dq}A_{dd}$ the integral Eq. (24) can be rewritten, to make all the Gaussian integrals explicit

$$I = -\frac{4v^2 A}{\pi^2} \int\limits_{-\infty}^{+\infty}\int\limits_{-\infty}^{+\infty} \mathrm{d}^2 s_q \mathrm{d}^2 s'_q\, e^{-2v\left(s_q^2 + s_q'^2\right)} \prod_k\prod_l e^{-c_{kl}\left(\vec{b} - \vec{s}_k + \vec{s}'_l\right)^2}\,, \tag{25}$$

where the abbreviations $c_{kl} = S_{kl}^{-2}$ refer to the coefficients in Eq. (17). Finally, the four Gaussian integrals have to be evaluated in our last expression Eq. (25), which leads to

$$I = -\frac{4v^2 A}{B} e^{-b^2 \frac{\Gamma}{B}}\,, \tag{26}$$

where

$$B = C_{qd,dq}\left(v + c_{qq} + \lambda^2 c_{dd}\right) + (1 - \lambda)^2 D_{qd,dq}\,,$$
$$\Gamma = C_{qd,dq}D_{qq,dd} + C_{qq,dd}D_{qd,dq}\,, \tag{27}$$

8

and

$$C_{kl,mn} = 4v + (1 + \lambda)^2 \left(c_{kl} + c_{mn}\right),$$
$$D_{kl,mn} = v \left(c_{kl} + c_{mn}\right) + (1 + \lambda)^2 c_{kl} c_{mn}.$$
(28)

Each term in Eq. (13) can be obtained from the master formula Eq. (26), by setting one or more coefficients to zero, $c_{kl} = 0$ and the corresponding amplitude to one, $A_{kl} = 1$.

Up to now, according to Eq. (5) and Eq. (6), $t_{el}(s, b)$ is purely imaginary and $\Omega(s, b)$ is real. Now we have to specify the imaginary part of the opacity function, that determines the real part of the FSA. Here several model assumptions are possible, but from the analysis of the ISR data and the first studies of the 7 TeV TOTEM data at LHC we learned, that the real part of the FSA is perturbatively small at ISR energies, it becomes non-perturbative at LHC but the scattering is still dominated by the imaginary part of the scattering amplitude.

We have studied several possible choices. One possibility is to introduce the imaginary part of the opacity function so that it is proportional to the probability of inelastic scatterings, which is known to be a decreasing function of the impact parameter b. A possible interpretation of this assumption may be that the inelastic collisions arising from non-collinear elastic collisions of quarks and diquarks follow the same spatial distributions as the inelastic collisions of the same constituents

$$\operatorname{Im}\Omega(s, b) = -\alpha \cdot \tilde{\sigma}_{inel}(s, b),$$
(29)

where α is a real number.

For the $\alpha = 0$ case, one recovers the $p = (q, d)$ version of the BB model of Ref. [1], while in the $|\alpha| \ll 1$ perturbative limit the αBB model of Ref. [3] is obtained (but note the that the values of the parameter α in the two models need to be correspondingly re-scaled).

The above proportionality between $\operatorname{Im}\Omega(s, b)$ and $\tilde{\sigma}_{inel}(b)$ in formula (29) provided the best fits from among the relations that we have tried. For example, we have also investigated the assumption that the real and the imaginary parts of the opacity function are proportional to one another

$$\operatorname{Im}\Omega(s, b) = -\alpha \cdot \operatorname{Re}\Omega(s, b).$$
(30)

However, as the results using Eq. (30) were less favorable as the results obtained with Eq. (29), we do the data analysis part, described in the next section, using Eq. (29). We mention this possibility to highlight that here some phenomenological assumptions are necessary as the ReBB model does allow for a broad range of possibilities for the choice of the imaginary part of the opacity function.

In this way, the ReBB model is fully defined, and at a given colliding energy only six parameters determine the differential (10) and total cross-sections (11) and also the ρ parameter, defined with Eq. (12). The parameters that have to be fitted to the data include the three scale parameters, R_q, R_d, R_{qd}, that

fix the geometry of the proton-proton collisions, as well as the three additional parameters α, λ and A_{qq}. Two of the latter three can be fixed: $\lambda = 0.5$ if the diquark is very weakly bound, so that its mass is twice as large as that of the valence quark, while $A_{qq} = 1$ suggests that head-on qq collisions are inelastic with a probability of 1. Thus in the actual data analysis only four parameters are fitted to the data at each $\sqrt{s}$: the three scale parameters R_q, R_d and R_{qd}, as well as the parameter α. As we shall see, the parameter α will play a key role when describing the shape of the dip of the differential cross-sections of elastic pp scatterings at LHC energies.

3 Fit method and results

The proton-proton elastic differential cross-section data measured by the LHC TOTEM experiment at 7 TeV is a compilation of two subsequent measurements [8, 9]. The squared four-momentum transfer value $t_{sep} = -0.375$ GeV^2 separates the two data sets.[1] Note, that the two datasets were taken with two different settings of the machine optics of the LHC accelerator.

The ReBB model, defined with Eq. (10), was fitted to the data at ISR energies and at LHC energy of $\sqrt{s} = 7$ TeV. The relation between the imaginary part of $\Omega(s, b)$ and α is defined with Eq. (29). In agreement with our previous investigations the $A_{qq} = 1$ and $\lambda = \frac{1}{2}$ parameters can be kept constant, which reduces the number of free parameters to four R_{qd}, R_q, R_d and α.

First we have attempted to fit the ReBB model in the $0 < |t| < 2.5$ GeV^2 range, fitting simultaneously both the low-$|t|$ and the dip region. In the course of the minimization of the ReBB model at $\sqrt{s} = 7$ TeV in this t-range, covering the two different TOTEM data sets, we found that the χ^2/NDF value decreases significantly, if a relative normalization constant γ is introduced between the fit of the two data sets. Therefore, the calculated differential cross-section is fitted with

$$\frac{\mathrm{d}\sigma}{\mathrm{d}t} \to \gamma \cdot \frac{\mathrm{d}\sigma}{\mathrm{d}t} \, , \tag{31}$$

if $|t| < |t_{sep}|$, where γ is an additional parameter to be minimized. The fit at $\sqrt{s} = 7$ TeV is shown in Fig. 1.

Although the fit looks reasonable and reproducing the data qualitatively rather well, the fit quality it is not yet statistically acceptable, when the fit is extended to the whole t-region of the combined data set. Note that we determined the fit quality using statistical errors only, and as claimed in the original TOTEM publications [8, 9], the systematic errors in the two data set might be slightly different, that is rather difficult to handle correctly in the present analysis. So instead of determining the systematic errors of the model parameters from the systematic errors of the data we decided to analyze the two TOTEM data sets separately and check for the consistency of the results. As detailed below, this strategy lead to a reasonable fit qualities (CL = 2.6 %,

---

[1]The squared four-momentum transfer value t_{sep} separates the bin centers at the common boundary, the two bins actually overlap [8, 9].

statistically acceptable fit in the cone region and CL = 0.04 %, statistically marginal fit in the dip region) with a remarkable stability of fit parameters as detailed below.

$\sqrt{s}$ [GeV]	23.5	30.7	52.8	62.5	7000	
$\|t\|$ [GeV^2]		(0, 2.5)			$(0, \|t_{sep}\|)$	$(\|t_{sep}\|, 2.5)$
χ^2/NDF	124.7/102	95.9/47	100.1/48	76.6/47	109.9/83	120.42/73
CL [%]	6.3	3×10^{-3}	2×10^{-3}	0.41	2.6	4×10^{-2}
R_q [fm]	0.27±0.01	0.28±0.01	0.27±0.01	0.28±0.01	0.45±0.01	0.43±0.01
R_d [fm]	0.72±0.01	0.74±0.01	0.74±0.01	0.75±0.01	0.94±0.01	0.91±0.01
R_{qd} [fm]	0.30±0.01	0.29±0.01	0.33±0.01	0.32±0.01	0.33±0.01	0.37±0.02
α	0.03±0.01	0.02±0.01	0.04±0.01	0.04±0.01	0.12	0.12±0.01

Table 1: The values of the fitted ReBB model parameters. The proton-proton elastic $d\sigma/dt$ data measured by the TOTEM experiment at 7 TeV is a composition of two subsequent measurements, which can be separated at t_{sep}. The overall fit involving the whole $0 < |t| < 2.5$ GeV^2 range provides $\chi^2/NDF = 336.4/159$ which is not statistically acceptable, while the fits below and above $|t_{sep}|$ provide either a statistically acceptable (CL > 0.1%) or marginally good (CL = 0.04%) fit quality.

If a *separated* fit to $\sqrt{s} = 7$ TeV elastic differential cross-section $d\sigma/dt$ data is evaluated, below and above the separation $|t_{sep}|$, a quality result can be obtained, which is shown in Figs. 2 and 3 and reported in Table 1, together with our results at ISR energies [8,9,18,19]. Note that the normalization factor γ, introduced in Eq. (31), is not applied at $\sqrt{s} = 7$ TeV, as the two data set were fitted separately.
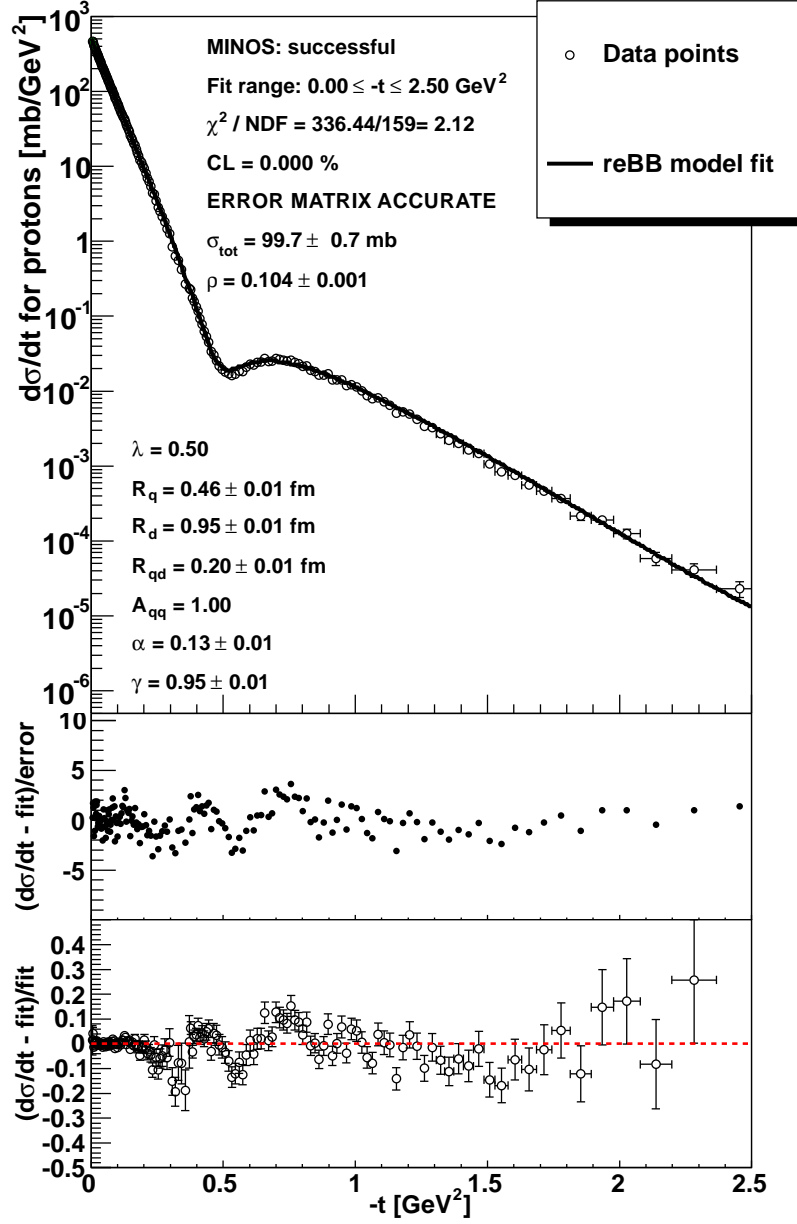
Figure 1: The fit of the ReBB model at $\sqrt{s} = 7$ TeV in the $0 < |t| < 2.5$ GeV^2 squared four momentum $|t|$ range. The real part of the amplitude t_{el} is defined with expression Eq. (29). According to Eq. (31) we use a relative normalization constant γ between the two TOTEM datasets at $\sqrt{s} = 7$ TeV. The fitted parameters are shown in the left bottom corner, parameters without errors were fixed in the minimization. The total cross-section σ_{tot} and the parameter ρ are derived quantities according to Eqs. (11) and (12), respectively.
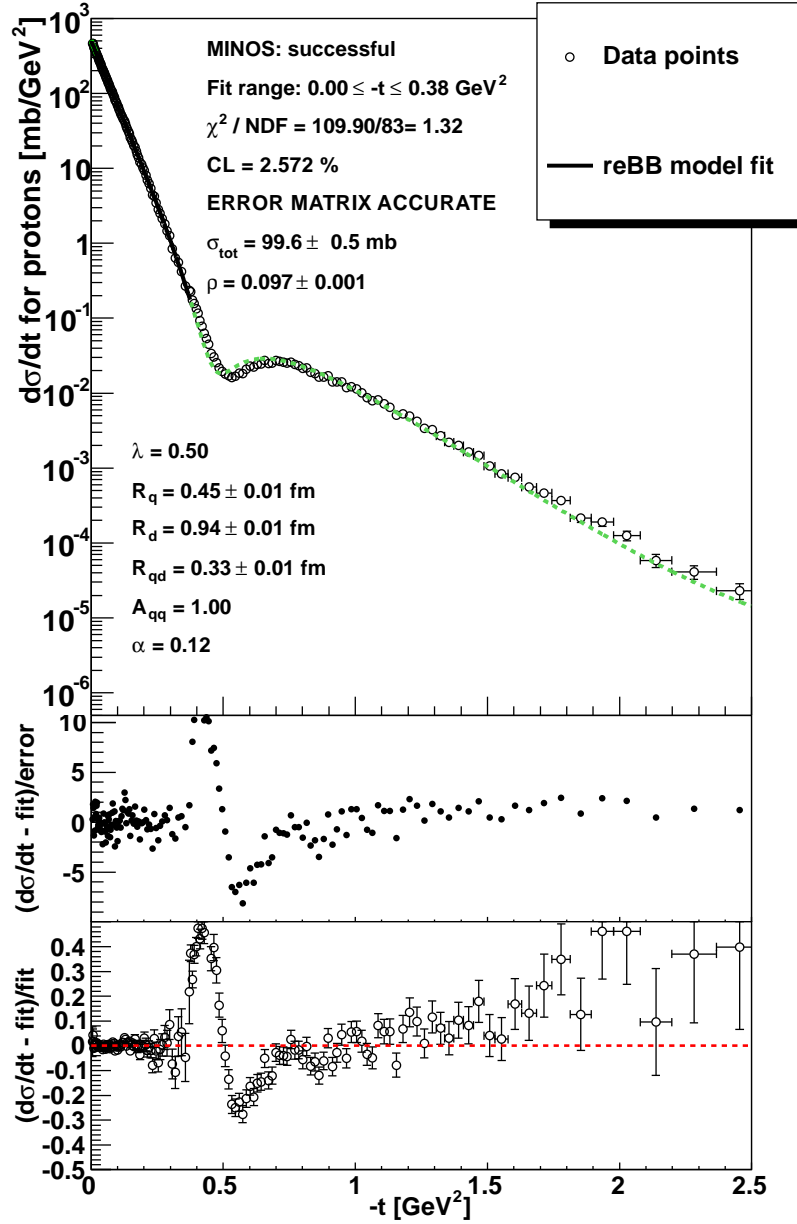
Figure 2: The same as Fig. 1, but the fit is evaluated in the $0 < |t| < |t_{sep}|$ range. The fitted curve is shown with solid line, its extrapolation above $|t_{sep}|$ is indicated with a dashed line. Note that the extrapolated curve remains close to the data points, following the measured differential cross-sections well even far away from the region where the model was fitted to the data.

13

p+p → p+p, diquark as a single entity at √s=7000.0 GeV

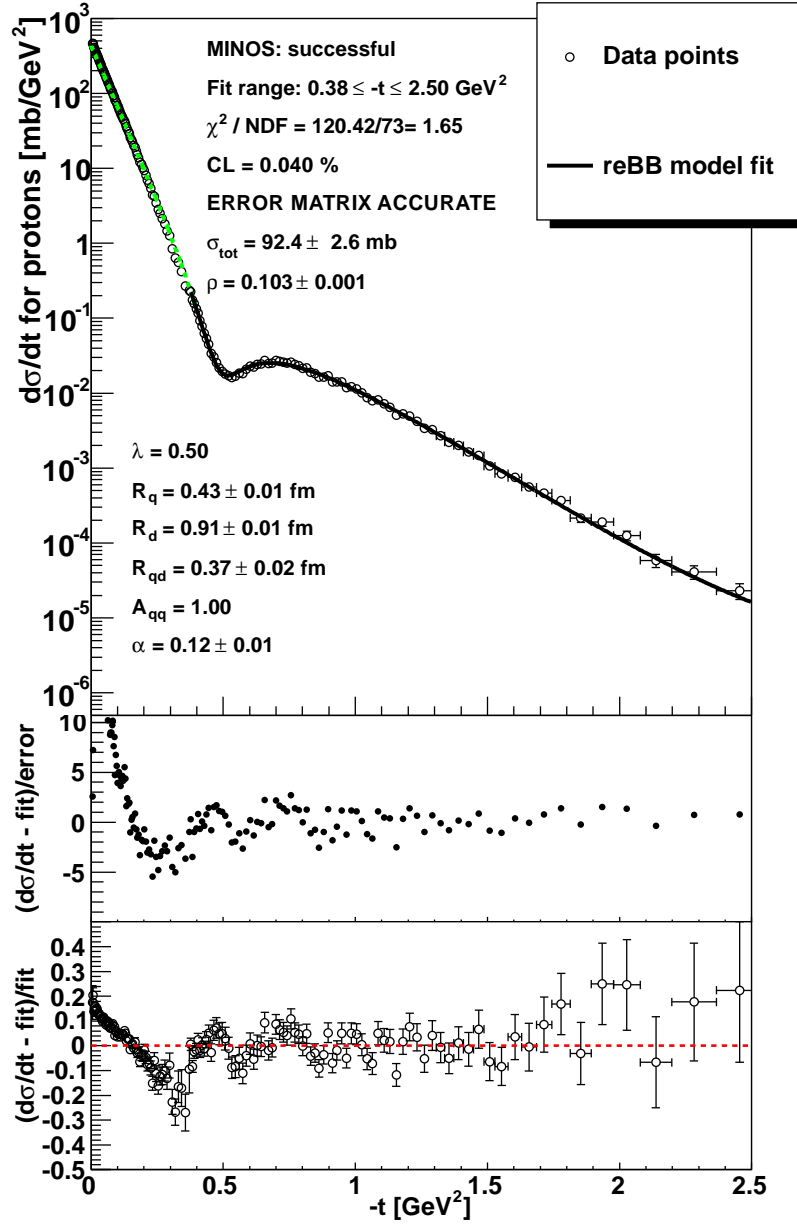dσ/dt for protons [mb/GeV^2]

10^3
10^2
10
1
10^{-1}
10^{-2}
10^{-3}
10^{-4}
10^{-5}
10^{-6}

MINOS: successful

Fit range: 0.38 ≤ -t ≤ 2.50 GeV^2

χ^2 / NDF = 120.42/73= 1.65

CL = 0.040 %

ERROR MATRIX ACCURATE

σ_{tot} = 92.4 ± 2.6 mb

ρ = 0.103 ± 0.001

λ = 0.50

R_q = 0.43 ± 0.01 fm

R_d = 0.91 ± 0.01 fm

R_{qd} = 0.37 ± 0.02 fm

A_{qq} = 1.00

α = 0.12 ± 0.01

○ Data points

—— reBB model fit

(dσ/dt - fit)/error

10
5
0
-5

(dσ/dt - fit)/fit

0.4
0.3
0.2
0.1
0
-0.1
-0.2
-0.3
-0.4
-0.5

0   0.5   1   1.5   2   2.5

-t [GeV^2]

Figure 3: The same as Fig. 1, but the fit is performed in the $|t_{sep}| < |t| < 2.5$ GeV^2 range. The fitted curve is shown with solid line, its extrapolation is indicated with a dashed line. Note that when the curve is extrapolated to the low-$|t|$ region, the extrapolated curve again follows the measured differential cross-section remarkably well even far away the fit region: the ReBB model fit is remarkably stable over the whole $|t|$-range.

14

The resulting parameters coming from the two separate fits at 7 TeV $d\sigma/dt$, over and below the $|t_{sep}|$ value, are *consistent* with each other within 2σ error. Note that at $\sqrt{s} = 7$ TeV the dip is not part of the fit range $(0, |t_{sep}|)$, thus the minimization procedure cannot determine the value of parameter α. In this case we have fixed α to the value of the fit from the other $|t|$ range above $|t_{sep}|$. The MINUIT status of the fit is successful in both cases.

Due to the stability of the fit parameters the extrapolation of the fit curves to the not fitted $|t|$ range remains close to the data points. The stability and consistency of the model description is visible in Fig. 2 and 3.

The calculated total cross-section of the low-$|t|$ fit $\sigma_{tot} = 99.6\pm0.5$ mb, where the uncertainty is the propagated uncertainty of the fit parameters, agrees well with the value $\sigma_{tot} = 98.0 \pm 2.5$ mb measured by the TOTEM experiment at $\sqrt{s} = 7$ TeV [10].

The parameter ρ can be better estimated from the fit over $|t_{sep}|$ which includes the dip. As the measured value of the ρ parameter $\rho = 0.145 \pm 0.091$ has large uncertainty the $\rho = 0.103 \pm 0.001$ calculated from the ReBB model is consistent with the measurement, see Fig. 2.

Also note that if $\mathrm{Im}\,\Omega(s, b)$ is defined to be proportional to $\mathrm{Re}\,\Omega(s, b)$, according to Eq. (30), the MINUIT fit result of $\chi^2/NDF = 405.6/159 = 2.55$ is obtained at $\sqrt{s} = 7$ TeV, which is disfavored as compared to fits with Eq. (29).

In our introduction we shortly mentioned the $p = (q, (q, q))$ version of the ReBB model, when the diquark is assumed to be a composition of two quarks [3]. This scenario provides a fit results with $\chi^2/NDF = 15509/159 \approx 97.5$, which means that the $p = (q, (q, q))$ ReBB version can be clearly rejected. The failure of this version is basically due the wrong shape of the differential cross-section: the second diffractive minimum appears too close to the first one.
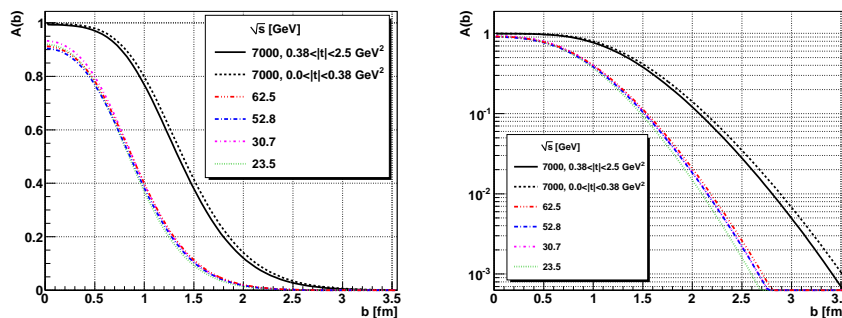

Figure 4: The shadow profile functions $A(b)$ indicate a saturation effect at LHC, while at ISR energies a Gaussian shape can be observed. Note that the dashed black curve is based on the statistically acceptable fit result in the $0 < |t| < 0.38$ GeV^2 range. The distributions' edge shows approximately the same width at each energy, corresponding to a constant "skin-width" of the proton.

4 Discussion

4.1 Shadow profile functions and saturation

The fits, from which the model parameters were determined, also permit us to evaluate the shadow profile function

$$A(s,b) = 1 - |\exp\left[-\Omega(s,b)\right]|^2 . \tag{32}$$

The obtained curves to $A(b)$ are shown in Fig. 4. The shadow profile functions at ISR energies exhibit a Gaussian like shape, which smoothly change with the center of mass energy $\sqrt{s}$. At LHC something new appears: the innermost part of the distribution shows a saturation, which means that around $b = 0$ the function becomes almost flat and stay close to $A(b) \approx 1$. Consequently, the shape of the shadow profile function $A(b)$ becomes non-Gaussian and somewhat "distorted" with respect to the shapes found at ISR.

At the same time the width of the edge of the shadow profile function A(b), which can be visualized as the proton's "skin-width", remains approximately independent of the center of mass energy $\sqrt{s}$.

4.2 Non-exponential behavior of $d\sigma_{el}/dt$

To compare the obtained ReBB fit with a *purely* exponential distribution the following exponential parametrization is used

$$\frac{d\sigma_{el}}{dt} = \left.\frac{d\sigma_{el}}{dt}\right|_{t=0} \cdot e^{-B \cdot |t|} , \tag{33}$$

where $d\sigma_{el}/dt|_{t=0} = 506.4$ mb/GeV^2 and slope parameter $B = 19.89$ GeV^{-2} is applied, according to the TOTEM paper Ref. [9].

The result, shown in Fig. 5, indicates a clear non-exponential behavior of the elastic differential cross-section in the $0.0 \le |t| \le 0.2$ GeV^2 range at $\sqrt{s} = 7$ TeV. Note that a similar non-exponential behavior was recently discussed by the TOTEM experiment [6] and also by the theoretical work of Ref. [7].

5 Extrapolation to future LHC energies and beyond

The ReBB model can be extrapolated to energies which have not been measured yet at LHC. The fit results of Table 1 and the parametrization

$$P(s) = p_0 + p_1 \cdot \ln\left(s/s_0\right) \tag{34}$$

is applied for each parameter $P \in \{R_q, R_d, R_{qd}, \alpha\}$, where $s_0 = 1$ GeV^2. The parametrization Eq. (34) implies that the four free parameters of the original ReBB model are replaced with eight parameters p_i. The fit of the ReBB parameters are shown in Fig. 6 and the fit parameters are collected in Table 2.
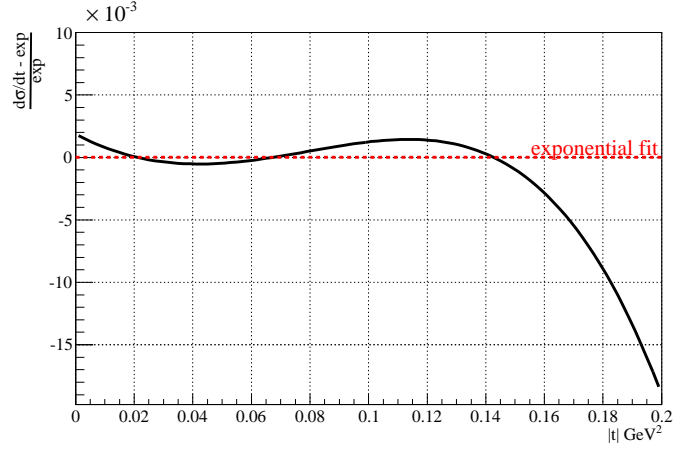
Figure 5: The ReBB model, fitted in the $0.0 \leq |t| \leq 0.36$ GeV^2 range, with respect to the exponential fit of Eq. (33). In the plot only the $0.0 \leq |t| \leq 0.2$ GeV^2 range is shown. The curve indicates a significant deviation from the simple exponential at low $|t|$ values.
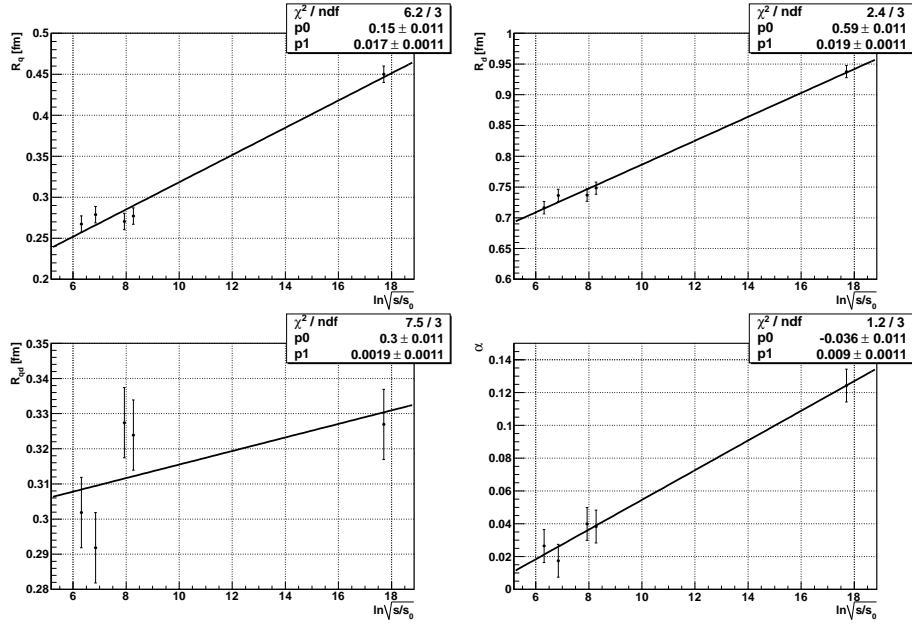

Figure 6: The results, collected in Table 1, are fitted with Eq. (34) for each parameter R_q, R_d, R_{qd} and α. The plots about the resulting fits are collected here, the parameters are collected in Table 2. The statistically acceptable quality of these fits allow the ReBB model to be extrapolated to center of mass energies which have not been measured yet at LHC.

17

The logarithmic dependence of the geometric parameters on the center of mass energy $\sqrt{s}$ in the parametrization Eq. (34) is motivated by the so-called "geometric picture" based on a series of studies [20–25].

Table 2 shows that the rate of increase with $\sqrt{s}$, parameter p_1, is an order of magnitude larger for R_q and R_d than for R_{qd}. The saturation effect, described in Section 4.1, is consistent with this observation as the increasing components of the proton, the quark and the diquark, are confined into a volume which is increasing more slowly.

Parameter	$R_q\ [fm]$	$R_d\ [fm]$	$R_{qd}\ [fm]$	α
χ^2/NDF	6.2/3	2.4/3	7.5/3	1.2/3
CL [%]	10.2	49.4	5.8	75.3
p_0	0.15 ± 0.01	0.59 ± 0.01	0.3 ± 0.01	-0.036 ± 0.01
p_1	0.017 ± 0.001	0.019 ± 0.001	0.0019 ± 0.001	0.009 ± 0.001

Table 2: Table 1 allows the extrapolation of the model parameters over the center of mass energy $\sqrt{s}$. The parametrization Eq. (34) is applied to extrapolate the ReBB model and the fits are shown in Fig. 6. The fit quality information is provided in the first and second row of the table. Note that the fit quality is acceptable for each parameter.

Using the extrapolation formula Eq. (34) and the value of the parameters from Table 2 it is straightforward to calculate the values of the parameters at expected future LHC energies of $\sqrt{s}$ =8, 13, 14, 15 TeV and also at 28 TeV, which is beyond the LHC capabilities. Using the extrapolated values of the parameters we plot our predicted pp elastic differential cross-section curves at each mentioned energy in Fig. 7. The shadow profile functions $A(b)$ can be also extrapolated, see Fig. 8. The shadow profile functions even allow us to visualize the increasing effective interaction radius of the proton in the impact parameter space in Fig. 9.

It is also important to see how the most important features change with center of mass energy $\sqrt{s}$: the extrapolated values of the total cross-section σ_{tot}, the position of the first diffractive minimum $|t_{dip}|$ and the parameter ρ is given in Table 3.
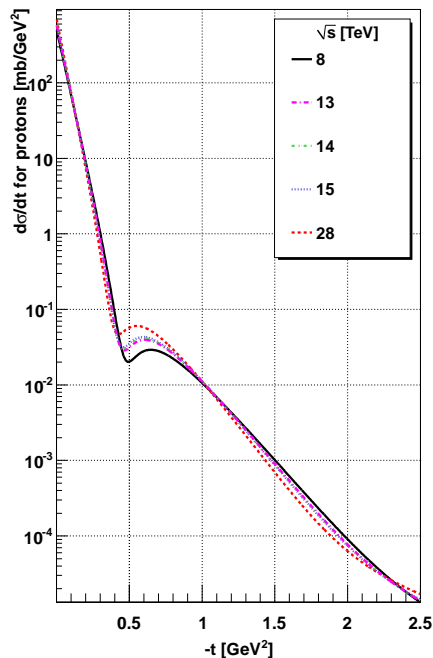

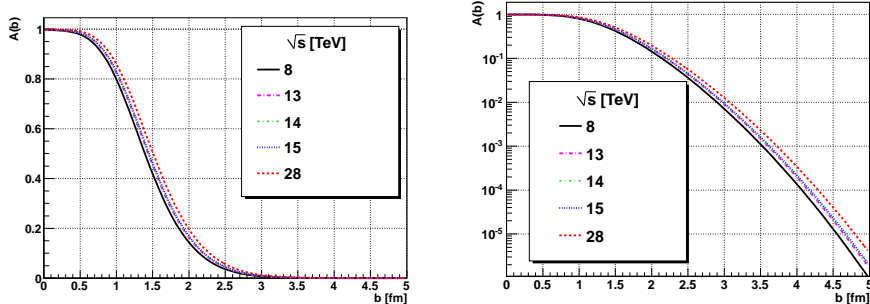Figure 7: The pp elastic differential cross-section is extrapolated to future LHC energies and beyond.

Figure 8: The shadow profile function at the extrapolated energies $\sqrt{s}$. The results show the increase of the proton interaction radius with increasing $\sqrt{s}$ energies. Also note that the "edge" of the distributions remains of approximately constant width and shape.

According to the results, the predicted value of $|t_{dip}|$ and σ_{tot} moves more than 10% when $\sqrt{s}$ increases from 8 TeV to 28 TeV, while the value of $C_{exp} = |t_{dip}| \cdot \sigma_{tot} \approx 49.8$ mb GeV^2 changes only about 2 %, which is an approximately constant value, within the errors of the extrapolation.

$\sqrt{s}$ [TeV]	σ_{tot} [mb]	$|t_{dip}|$[GeV^2]	ρ	$|t_{dip}| \cdot \sigma_{tot}$ [mb GeV^2]
8	100.1	0.494	0.103	49.45
13	107.1	0.465	0.108	49.8
14	108.1	0.461	0.108	49.83
15	109.1	0.457	0.109	49.86
28	118.5	0.426	0.114	50.48

Table 3: The extrapolated values of the total cross-section σ_{tot} at future LHC energies and beyond. The position of the first diffractive minimum $|t_{dip}|$, the parameter ρ and the $|t_{dip}| \cdot \sigma_{tot}$ value is also provided at each energy. Note that the predicted value of $|t_{dip}|$ and σ_{tot} moves more than 10% when $\sqrt{s}$ increases from 8 TeV to 28 TeV, while the value of $|t_{dip}| \cdot \sigma_{tot}$ changes only about 2%.

A similar, and exact, scaling can be derived for the case of photon scattering on a black disk, where the elastic differential cross-section is [26]

$$\frac{d\sigma_{black}}{dt} = \pi R^4 \left[\frac{J_1(q \cdot R)}{q \cdot R} \right]^2 , \tag{35}$$

where $t = -q^2$ and R is the radius of the black disk. The total cross-section is given by

$$\sigma_{tot,black} = 2\pi R^2 . \tag{36}$$

19

In this simple theoretical model the position of the first diffractive minimum, following from Eq. (35), and the total cross-section Eq. (36) satisfies

$$C_{black} = |t_{dip,black}| \cdot \sigma_{tot,black} = 2\pi j_{1,1}^2 (\hbar c)^2 \approx \ 35.9 \, \text{mb} \, \text{GeV}^2 \, , \qquad (37)$$

where $j_{1,1}$ is the first root of the first order Bessel-function of the first kind $J_1(x)$.

The scaling behavior indicated by the stability of the value C_{exp} is somewhat different from the black disk model, described by Eq. (37), as the corresponding value C_{black} is significantly different

$$C_{black} \neq C_{exp} \, . \qquad (38)$$

In this sense the value of C_{exp} indicates a more complex scattering phenomena, than the photon black disc scattering.

6   Summary and conclusions

The real part of the forward scattering amplitude (FSA) is derived from unitarity constraints in the Bialas-Bzdak model leading to the so-called ReBB model. The added real part of the FSA significantly improves the model ability to describe the data at the first diffractive minimum. In total the ReBB model describes both the ISR and LHC data in the $0 < |t| < 2.5$ GeV^2 squared momentum transfer range in a statistically acceptable manner; in the latter case the fit range has to be divided to two parts, according to the compilation of the two independent TOTEM measurements. The results are collected in Table 1.

The fit results also permit us to evaluate the shadow profile functions $A(b)$, see Fig. 4. The plots indicate a Gaussian shape at ISR energies, while at LHC a saturation effect can be observed: the innermost part of the shadow profile function $A(b)$ around $b = 0$ is almost flat and close to $A(b) \approx 1$. The elastic differential cross-section can be compared to a purely exponential distribution and the comparison shows a significant deviation from pure exponential in the $0.0 \leq |t| \leq 0.2$ GeV^2 range.

The fit results allow the determination of the excitation functions of the ReBB model at future LHC energies and beyond, with parameters collected in Table 2 and predicted differential cross-section curves shown in Fig. 7. The shadow profile functions can be also extrapolated, see Fig. 8, which predicts that the saturated part of the proton is expected to increase with increasing center of mass energy $\sqrt{s}$. The edge of the distribution, the "skin-width" of the proton, expected to remain approximately constant. It is worth to mention that the extrapolated version of the ReBB model utilizes of only eight parameters, the p_i parameters of Table 2, and in this sense a "minimal" set of parameters is applied.
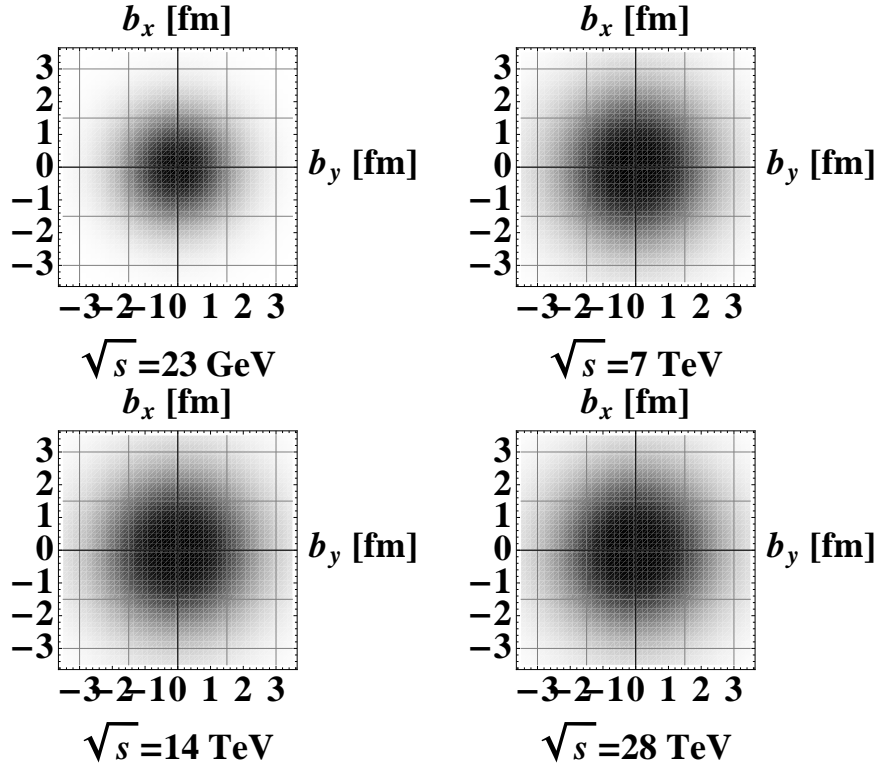
Acknowledgement

Figure 9: Visualization of the shadow profile functions $A(b)$ in the transverse plane of the impact parameter vector (b_x, b_y). The figures show the increase of the proton effective interaction radius in the impact parameter space with increasing center of mass energy $\sqrt{s}$. It can be also observed that the black innermost core of the distributions is increasing, while the thickness of the proton's "skin", the gray transition part of the distributions, remains approximately independent of the center of mass energy $\sqrt{s}$.

References

[1] A. Bialas and A. Bzdak, Acta Phys. Polon. B **38** (2007) 159 [hep-ph/0612038].

[2] F. Nemes and T. Csörgő, Int. J. Mod. Phys. A **27** (2012) 1250175

[3] T. Csörgő and F. Nemes, Int. J. Mod. Phys. A **29** (2014) 1450019

[4] E. Ferreira, T. Kodama and A. K. Kohara, arXiv:1411.3518 [hep-ph].

[5] A. K. Kohara, E. Ferreira and T. Kodama, Eur. Phys. J. C **74** (2014) 11, 3175 [arXiv:1408.1599 [hep-ph]].

[6] S. Giani, "Overview of TOTEM results on total cross-section, elastic scattering and diffraction at LHC", talk given at WPCF 2014, Gyöngyös, Hungary, August 2014, `https://indico.cern.ch/event/300974/session/2/contribution/34` .

[7] L. Jenkovszky and A. Lengyel, arXiv:1410.4106 [hep-ph].

[8] G. Antchev *et al.*TOTEM Collaboration, Europhys. Lett. **96** (2011) 21002

[9] G. Antchev *et al.* [TOTEM Collaboration], Europhys. Lett. **101** (2013) 21002.

[10] G. Antchev *et al.* [TOTEM Collaboration], Europhys. Lett. **101** (2013) 21004.

[11] R. J. Glauber, Lectures in Theoretical Physics, Vol. 1. Interscience, New York 1959.

[12] E. Levin, hep-ph/9808486.

[13] V. A. Khoze, A. D. Martin and M. G. Ryskin, arXiv:1402.2778 [hep-ph].

[14] M. G. Ryskin, A. D. Martin and V. A. Khoze, Eur. Phys. J. C **72** (2012) 1937 [arXiv:1201.6298 [hep-ph]].

[15] M. G. Ryskin, A. D. Martin, V. A. Khoze and A. G. Shuvaev, J. Phys. G **36** (2009) 093001 [arXiv:0907.1374 [hep-ph]].

[16] A. D. Martin, H. Hoeth, V. A. Khoze, F. Krauss, M. G. Ryskin and K. Zapp, PoS QNP **2012** (2012) 017

[17] P. Lipari and M. Lusignoli, Eur. Phys. J. C **73**, 2630 (2013) [arXiv:1305.7216 [hep-ph]].

[18] E. Nagy, R. S. Orr, W. Schmidt-Parzefall, K. Winter, A. Brandt, F. W. Busser, G. Flugge and F. Niebergall *et al.*, Nucl. Phys. B **150** (1979) 221.

[19] U. Amaldi and K. R. Schubert, Nucl. Phys. B **166** (1980) 301.

[20] H. Cheng and T. T. Wu, Phys. Rev. Lett. **22** (1969) 666.

[21] H. Cheng and T. T. Wu, Phys. Rev. **182** (1969) 1852.

[22] H. Cheng and T. T. Wu, Phys. Rev. **182** (1969) 1868.

[23] H. Cheng and T.T. Wu, Expanding Protons: Scattering at High Energies , M.I.T. Press, Cambridge, MA (1987)

[24] C. Bourrely, J. Soffer and T. T. Wu, Phys. Rev. D **19** (1979) 3249.

[25] C. Bourrely, J. Soffer and T. T. Wu, arXiv:1405.6698 [hep-ph].

[26] M. M. Block, Phys. Rept. **436** (2006) 71 [hep-ph/0606215].